Laser vaporized Li_2, Na_2, K_2, and LiNa molecules observed by cavity ring-down spectroscopy

I. Labazan and S. Milošević
Institute of Physics, P.O. Box 304, HR-10000 Zagreb, Croatia
(Received 10 March 2003; published 19 September 2003)

Laser ablation of solid lithium, sodium, potassium, and lithium-sodium alloy was performed using a 308-nm excimer laser at fluences close to 1 J cm^{-2}. Frequency and time resolved *A-X* and *B-X* electronic transitions of $^{6,7}Li_2$, Na_2, LiNa and K_2 respectively, were observed. Lithium atom, dimer velocities, and influence of the background gas on dimer content of the plume have been measured. The origin of dimers at high densities, with subthermal internal energy, is discussed.

DOI: 10.1103/PhysRevA.68.032901 PACS number(s): 79.20.Ds, 52.38.Mf, 33.20.Kf

I. INTRODUCTION

Cooling and trapping of molecules for creation of Bose condensates is a demanding task, and one of the key technical challenges is how to efficiently prepare molecules at the high densities and low internal energies required for condensation. Laser vaporization (or ablation) is a distinctive nonthermal process resulting in a plume in which different interactions between contents are possible. These plumes have been shown to facilitate the formation of different molecules and molecular ions which cannot be produced by other means such as ovens or cells. Our particular interest comprises dimers containing alkali-metals particularly lithium such as LiC or LiSi, which according to calculations should be stable in particular electronic states, but have not yet been experimentally observed [1]. Because the component elements possess quite different vapor pressures and melting points they cannot be produced in heat-pipe ovens, for example Refs. [2,3].

Laser ablation or vaporization of alkali-metal targets is of interest in various research fields [4–7]. The content of the plume has been well studied in respect of atoms and ions [8–10]. However, dimer observation has been reported in only a few cases for lithium and sodium [11–15], while, to the best of our knowledge, potassium dimers have not yet been observed in laser-vaporization plumes. Usually, very bright emission from the plume shows only contributions from ions and excited atoms and not excited molecules [10]. Therefore, employment of a direct absorption technique such as cavity ring-down spectroscopy (CRDS) is needed [15].

Primarily, this paper is concentrated on the detection and study of alkali-metal dimers in plumes from pure and mixed alkali-metal targets. We observed dimers of lithium, sodium, and potassium, as well as mixed LiNa molecules in excimer laser-vaporized plumes of solid alkali-metal targets. Absorption cross sections were theoretically calculated and used to determine dimer densities. Problems in resolving different overlapping spectral features in the case of mixed targets were avoided by choosing appropriate detection regions with the help of quantum-mechanical calculations. The content of the plume was studied with respect to laser fluence and background gas pressure.

II. EXPERIMENT

The principle of conventional pulsed CRDS is quite simple [16,17]. A short laser pulse is coupled into a stable high finesse optical cavity. A small amount of intensity leaks out of the cavity and is detected as a function of time (so-called ring-down curve). A ring-down curve is described by a single-exponential decay function in the ideal case of linear absorption and validation of the Beer-Lambert law. It is characterized by a lifetime τ of photons in the cavity. Usually, one measures total cavity loss $\beta(\lambda)/c \equiv (1/c)(1/\tau)$ expressed in units of cm^{-1}. Neglecting other losses, the absorption coefficient is then given by

$$k(\lambda) = \frac{L}{l_{abs}} \frac{[\beta(\lambda) - \beta_0(\lambda)]}{c} \equiv \sigma(\lambda) N, \tag{1}$$

where L is the cavity length, λ is the wavelength, l_{abs} is the single-pass absorption length, and $\beta(\lambda)$ and $\beta_0(\lambda)$ are losses in the cavity with or without the absorption sample, respectively. $\sigma(\lambda)$ is the absorption cross section and N is the density of absorbing molecules. Thus one can determine the density of absorbing molecules or atoms from the measured absorption coefficients, provided that relevant absorption cross sections are known.

The application of CRDS to ablation plumes introduces a complication due to change of the ablated particle densities during the ring-down time. In this case the time-dependent absorption coefficient is

$$k(\lambda, t) = -\frac{L}{c l_{abs}} \left\{ \frac{d}{dt} \left[\ln\left(\frac{S(t)}{S_0} \right) \right] - (1 - R) \right\}, \tag{2}$$

where $S(t)$ is the ring-down signal at time t and S_0 the ring-down signal at $t = 0$. $1 - R$ is the effective mirror loss [18,19]. Recently we employed a temporally resolved CRDS technique using a fitting procedure involving a series of time windows across the ring-down curve [15]. Evaluation in subsequent time windows and application of Eq. (1) were shown to have certain advantages with respect to signal-to-noise ratio [20].

The experimental setup is shown in Fig. 1. Laser ablation was performed within the vacuum chamber which could be evacuated by means of either a roots pump system or a diffusion pump yielding final pressures of about 10^{-3} or 10^{-6} Torr, respectively. The laser system consists of an excimer (LPX 105E Lambda Physik) pumped dye laser (LPD 3002E Lambda Physik) working with a DCM dye. The laser pulse duration was about 15 ns and bandwidth about 6 GHz.

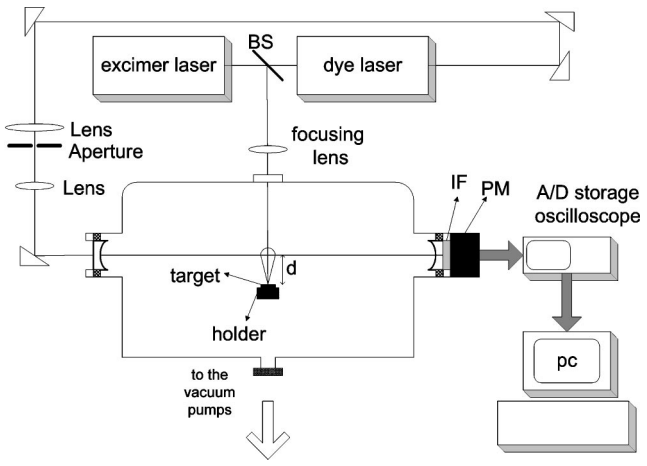

FIG. 1. Experimental arrangement for CRDS on a laser-vaporized plume. BS, beam splitter; IF, interference filter; and PM, photomultiplier.

Part of the 308-nm beam normally used for pumping the amplifier stage was used to produce ablation perpendicular to the target surface or at 35°. Targets of solid alkali metal (99.9% purity, of natural isotope abundance for Li and K) were mounted on an *X-Y* translation stage to allow precise positioning (100 μm). Targets were also rotated to avoid drilling.

Cavity mirrors were mounted on the vacuum chamber by means of special holders which allowed easy cavity adjustment. The mirror radius of curvature was 0.5 m and the reflectivity was about 99.997% in the spectral range 600–690 nm. The cavity length was 0.851 m and typical cavity ring-down times were 30–40 μs (i.e., the time in which cavity signal falls to 1/*e* of initial value). The calculated waist for TEM_{00} was 0.037 cm in the center of the cavity, and by obstructing the cavity path we were able to measure the actual waist to be 0.095 cm.

For CRDS, only the oscillator/preamplifier stage of the dye laser was used. The optical arrangement was such that the time delay between the 308-nm ablation beam and the dye laser beam at the target position was 10 ns. The laser pulse energy of the CRDS laser was about 1 μJ measured in front of the entrance cavity mirror. The laser ablation beam had a pulse energy of about 10 mJ. The spot surface on the target was in the range from 0.7×10^{-2} to 2×10^{-2} cm^2 and was varied by moving a quartz lens (33.5 cm focal length) towards or from the target. The surface area illuminated by the laser was determined prior to the experiment by measuring the sizes of burn marks on black paper using a microscope.

Detection of the ring-down signals was performed by a photomultiplier (RCA C31034). An optical cutoff filter or appropriate interference filters were placed between the end-cavity mirror and the photomultiplier to stop UV and IR light from the laser-induced plume. An 8-bit, 150-MHz digital oscilloscope (HAMEG 1507-1) was used to measure the CRDS decay curves, which were stored in a PC for further analysis. Stored ring-down decays were analyzed in selected time intervals by performing exponential fitting using a least-square method.

We also examined laser ablation of the mixed alkali metals. For this purpose we prepared sodium-lithium alloys in a heat-pipe oven [21]. Approximately equal amounts of solid lithium and sodium are put in a special target holder, and were put in a heat pipe with 760 Torr of helium and heated up to 720 K for about an hour. Such conditions seem sufficient for complete mixing of sodium and lithium liquids. After cooling to room temperature, this mixed target could be used in the ablation experiment.

III. RESULTS

A. Spectral simulations and density determination

For identification of experimentally observed spectral features and density determinations we calculated quantum-mechanical absorption cross sections for alkali-metal diatomic molecules. The averaged absorption cross section at some frequency ν for bound-bound transition is given by [22]

$$\sigma(\nu)=\frac{8\pi^3\nu}{3hc}\frac{1}{Z_{v'}Z_{J''}}\times\sum_{J'J''v'v''}g(\nu)\omega_{J''}|\langle\Phi_{v''J''\Lambda''}|D(R)|\Phi_{v'J'\Lambda'}\rangle|^2S^{J'\Lambda'}_{J''\Lambda''}\times\exp(-E/kT), \tag{3}$$

where $\omega_{J''}$ is the statistical factor due to the nuclear spin, $S^{J'\Lambda'}_{J''\Lambda''}$ is the Höln-London factor, and E is equal to the sum of dissociation energy D_e and rovibrational energy of the lower electronic state: $E=D_e+E_{rot,vib}(v'',J'',\Lambda'')$. $Z_{v''}$ and $Z_{J''}$ are vibration and rotation partition functions of the lower state, which are calculated in the harmonic approximation. $\Phi_{v'J'}$ and $\Phi_{v''J''}$ are solutions of the radial part of the Schrödinger equation for upper and lower electronic states and $D(R)$ is electronic dipole moment transition function. Potential-energy curves and electronic dipole moment functions were prepared as described below. Franck-Condon factors were calculated by solving the Schrödinger equation in Hund's case *a*, including only bound-bound transitions for the purpose of the present study. For the line profile $g(\nu)$ we assumed a normalized Gaussian. The full widths at half maximum, $\Delta\nu$, were chosen such that calculation fits the observed spectral line shape. Averaging was performed assuming Boltzmann distributions for both rotational and vibrational populations in the lower electronic state. First rotational averaging is performed for each $v''\rightarrow v'$ vibrational transition. Results were then vibrationally averaged.

Lithium potential-energy curves used in the calculations were constructed in a fashion similar to the procedure described in Ref. [23]. For the $^7Li_2$ ground state $X\,^1\Sigma_g^+$ and the first excited electronic state $A^1\Sigma_u^+$, Rydberg-Klein-Rees (RKR) potentials from Refs. [24,25], respectively, were used. For the electronic dipole transition moment function we used *ab initio* calculations from Ref. [26]. The same potential-energy curves and dipole moment function were used in the calculation of the $^6Li^7Li$ molecule absorption but with ap-

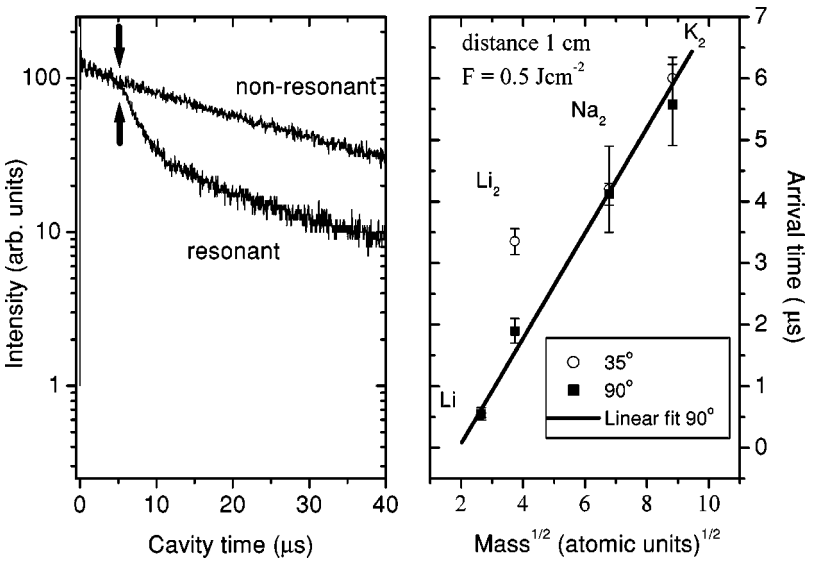

FIG. 2. Left: typical ring-down decay curves in semilogarithmic scale for the cases when laser wavelength was in and out of resonance with some molecular transition. Bold arrows show the moment at which particular molecular species arrive at the observation axis. Right: arrival times of alkali-metal atoms and dimers as a function of the square root of mass for $d=1$ cm and $F=0.5$ J cm^{-2}. The solid line represents a linear fit of the experimental data points for normal incidence.

propriate spectroscopic constants obtained from Ref. [27]. Calculations were done for ranges of lower and upper state vibrational numbers (0,10) and (0,25), respectively, with a maximum rotational number of 80 and $\Delta\nu=0.025$ nm.

The potential-energy curve for the $Na_2(X\,^1\Sigma_g^+)$ state was the inverted perturbation approach (IPA) potential [28] and for the $A^1\Pi_u$ we used the RKR potential from Ref. [29]. The *ab initio* electronic dipole transition moment function for the $Na_2(X^1\Sigma_g^+$-$A^1\Pi_u)$ transition from Ref. [30] was used and scaled as described in Ref. [31]. Ranges of lower and upper state vibrational numbers used in the calculation were (0,10) and (0,25), respectively, with a maximum rotational number equal to 100 and $\Delta\nu=0.02$ nm.

For the $K_2(X^1\Sigma_g^+-B^1\Pi_u)$ absorption cross-section calculation RKR potentials from Ref. [32] and the dipole moment from Ref. [33] were used. Calculations were performed for ranges of lower and upper state vibrational numbers (0, 41) and (0,30), respectively. The maximum rotational number was 150 and $\Delta\nu=0.02$ nm.

The accuracy of calculations with the above potentials was tested in Refs. [23] and [31] for Li_2 and Na_2, respectively. The quality of calculation for the potassium case was proved by excellent reproduction of the absorption spectrum given in Figure 7 of Ref. [34].

For the LiNa mixed dimers, the potential-energy curves and spectroscopic constants from Refs. [35,36] have been used. Calculations were performed for ranges of lower and upper state vibrational numbers (0, 25) and (0, 15), respectively. The maximum rotational number was 50 and $\Delta\nu=0.01$ nm. The dipole transition moment of the $X\,^1\Sigma^+-A\,^1\Pi$ band in LiNa is not available, and was set to unity in calculations.

The single-pass absorption length l_{aps} depends on the distance between the target surface and the cavity axis. The shape of the vaporized plume is well approximated by a cone with angle $\phi=40°$ [37], so that $l_{abs}=2d\tan\phi/2$. The angle $\phi=40°$ was also assured by inspection of the vaporized species deposited on the electrodes of the time-of-flight mass spectrometer mounted in the vacuum chamber [38] and by visual inspection of pictures taken with a charge coupled device camera. We assumed that density was uniform along the entire absorption length.

B. CRDS measurements

Figure 2 shows typical cavity decay curves at $d=1$ cm distance of the target from the cavity axis for the dye laser tuned off and on molecular resonance. When the dye laser was detuned from absorption, the ring-down curve was approximated by a simple straight line in a semilog plot. When the laser was tuned to the absorption, a complicated ring-down curve is obtained. In the first time interval the cavity was empty, i.e., absorbers did not arrive at the cavity axis. At some particular moment (arrival time) absorbers cross the axis and a different slope appears. After the absorbers leave the region of the cavity waist, the remaining photons exhibit the same slope as in the case of the detuned laser wavelength (or empty cavity). The right part of Fig. 2 shows arrival times for different alkali-metal dimers at $d=1$ cm. Values for 35° angle and normal incidence are similar within the accuracy of determination. Arrival time should be proportional to the square root of the atomic mass if all particles gain the same kinetic energy in the laser-vaporization process. The fit to such a dependence is shown by the solid line, supporting this assumption.

In Fig. 3(a) an absorption spectrum of the laser-vaporized lithium target in the wavelength range (664-672) nm is shown. Rotational progressions $v''=0\rightarrow v'=4$ within the $^6Li^7Li(X\,^1\Sigma_g^+$-$A\,^1\Sigma_u^+$, at 664.32 nm) and the $^7Li_2(X\,^1\Sigma_g^+$-$A\,^1\Sigma_u^+$, at 665.92 nm) electronic transitions were identified with the help of absorption cross-section calculations. The time window chosen for the determination of absorption loss starts 3.4 μs after the laser pulse for CRDS enters the cavity, and was 2.25 μs long. The atomic transition Li($2s$-$2p$) has been observed, but in the time window chosen for evaluation of molecular absorption, the ring-down curves for wavelength near the line center approach zero intensity. Therefore only line-wings of the $2s$-$2p$ transition are observed. Note that molecular transitions very close to the center of the atomic line could be measured using this

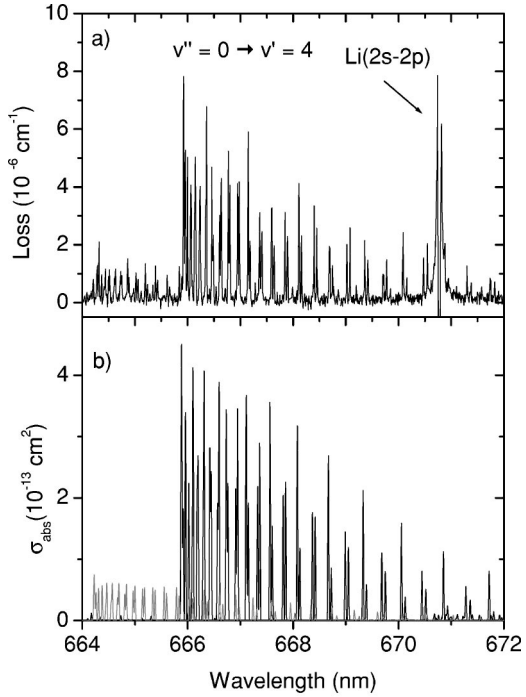

FIG. 3. (a) Typical cavity loss spectrum of the $Li_2(X\,^1\Sigma_g^+$-$A^1\Sigma_u^+)$ electronic transitions in the range (664–672) nm for the normal incidence of the laser ablation beam. $d=2$ cm, $F=0.84$ J cm^{-2}. (b) Quantum-mechanical calculation of the absorption cross section for $T_{rot}=T_{vib}=175$ K. Black line, the $^7Li_2(X\,^1\Sigma_g^+$-$A\,^1\Sigma_u^+)$ absorption cross section; and gray line, the $^6Li^7Li(X\,^1\Sigma_g$-$A\,^1\Sigma_u)$ absorption cross section.

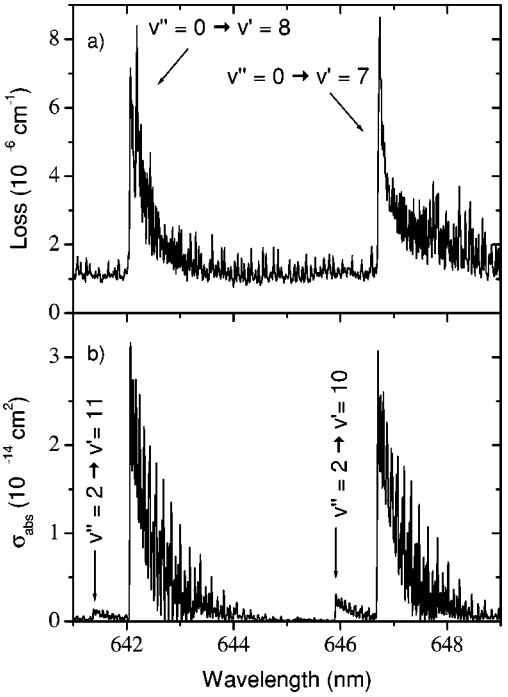

FIG. 4. Typical cavity loss spectrum of the $Na_2(X\,^1\Sigma_g^+$-$A\,^1\Sigma_u^+)$ electronic transitions in the range (641–649) nm. The angle of incidence equals 35°, $d=1$ cm, and $F=0.7$ J cm^{-2}. (b) Quantum-mechanical calculation of the absorption cross section for rotational and vibrational temperatures of 50 K and 350 K, respectively.

technique because the atoms are faster and are already gone in the time window shown. In addition, there are no significant collisions in the plume which could induce line broadening. The observation of the atomic line center was restricted to short and early time windows where large losses are observed. We did not analyze this further due to possible well-known bandwidth problems of CRDS at large absorbances [15]. Quantum-mechanical calculations of the molecular absorption cross section for $T_{rot}=T_{vib}=175$ K are presented in Fig. 3(b). The Li($2s$-$2p$) atomic transition was not included in these calculations. The natural abundance ratio of ^{7}Li to ^{6}Li isotopes is 93:7 and the expected ratio of dimers is $^7Li_2$:$^6Li^7Li$:$^6Li_2=1:0.1603:0.0064$. Calculated absorption cross sections are scaled in respect to this ratio. Comparison with observations shows that the fraction of $^6Li^7Li$ isotopomer within the plume is in accordance with natural abundance.

Figure 4(a) shows the loss spectrum of the laser-induced plume from a pure sodium target in the range (641–649) nm. The time window for evaluation starts 8.65 μs after the beginning of "ringing" with a duration of 3.45 μs. Rovibrational bands $v''=0\rightarrow v'=7,8$, $v''=2\rightarrow v'=10,11$ of the $Na_2(X\,^1\Sigma_g^+-A^1\Sigma_u^+)$ electronic transition are identified. In Fig. 4(b) the calculated absorption cross section for assumed rotational and vibrational temperatures equal to 50 K and 350 K, respectively, is shown. For these temperature values good agreement between the experimental spectrum and the calculated σ_{abs} is observed.

A typical cavity loss spectrum in the wavelength range (641–649) nm of the ablation plume from a pure solid potassium target is shown in Fig. 5(a). The time window chosen for loss determination starts 8 μs after the entrance of the laser pulse into the cavity and lasts for 4 μs. In Fig. 5(b) the calculated absorption cross section in the same wavelength region for $T_{rot}=T_{vib}=125$ K is shown. We identified the most intense vibrational-rotational bands within the $K_2(X\,^1\Sigma_g^+-B\,^1\Pi_u)$ electronic transition: $v''=0\rightarrow v'=1,2,3$, as indicated. Vibrational bands which are starting from vibrational levels 1 and 2 are also indicated in Fig. 5(b). They are not well resolved in the experiment.

From calculated absorption cross section and measured cavity losses, densities of observed alkalis in the plume at a given distance (time instance) from the target surface using Eq. (1) can be calculated. For example, at a distance $d=1$ cm, lithium dimer densities in the ablation plume are $\approx 1\times10^{10}$ cm^{-3} and 1.23×10^9 cm^{-3} for $^7Li_2$ and $^6Li^7Li$, respectively, while the densities of sodium and potassium dimers are $N(Na_2)=3\times10^{10}$ cm^{-3} and $N(K_2)=1.5\times10^{10}$ cm^{-3}, respectively. These densities correspond to the time interval in which the dimer density distribution has a maximum, as described above. We note that in all cases, the absorbances are sufficiently small to ensure that true absorption coefficients are extracted, as discussed in Refs. [39,40].

Analyzing Figs. 3–5, we see that the molecular spectra are more dense moving from lithium to potassium. This is due to the decrease of vibrational frequency ω_e as we go towards heavier molecules: 351.39 cm^{-1} for the $Li_2(X\,^1\Sigma_g^+)$ state, 159.1045 cm^{-1} for the $Na_2(X\,^1\Sigma_g^+)$ state and

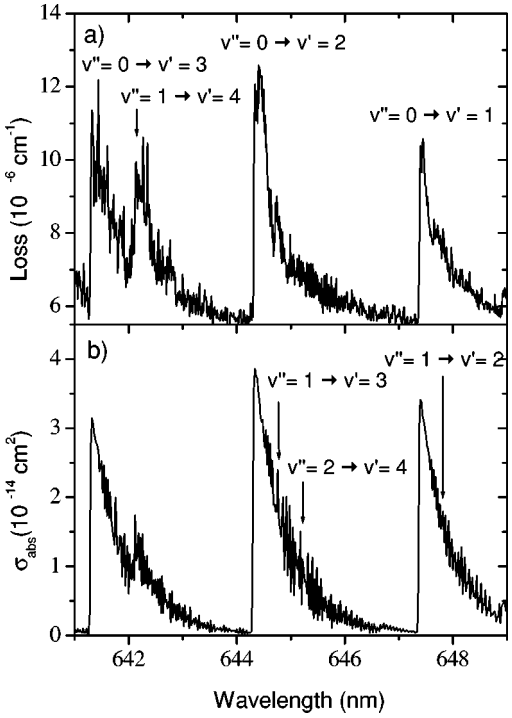

FIG. 5. Typical cavity loss spectrum of the $K_2(X\,^1\Sigma_g^+$-$B\,^1\Pi_u)$ electronic transitions in the range (641–649) nm. The angle of incidence is 35°, $d=1$ cm, and $F=0.7$ J cm^{-2}. (b) Quantum-mechanical calculation of absorption cross section for the $T_{rot}=T_{vib}=125$ K.

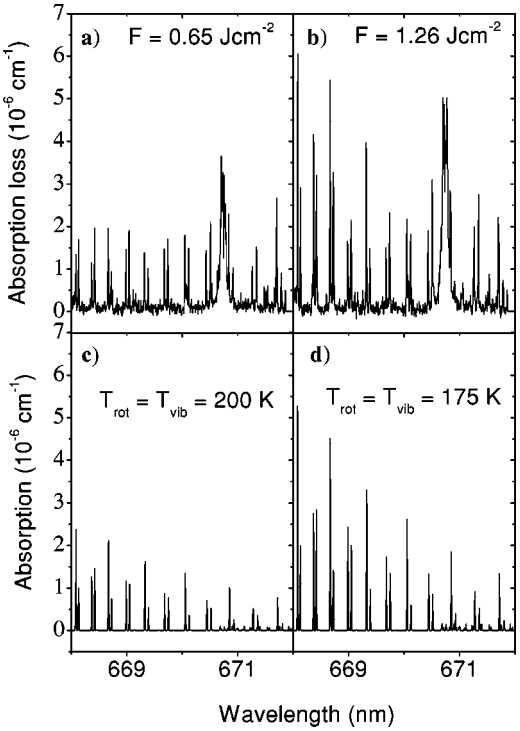

FIG. 6. Cavity absorption losses at laser fluences: (a) $F=0.65$ J cm^{-2}, (b) $F=1.26$ J cm^{-2}; and calculated absorption for (c) $T_{rot}=T_{vib}=200$ K, (d) $T_{rot}=T_{vib}=175$ K. The distance from the target surface to the cavity axis is 3 cm. The time window chosen for determination of cavity losses is (3.2–7.7) μs.

92.398 cm^{-1} for the $K_2(X\,^1\Sigma_g^+)$. We chose lithium for further investigations due to its well-resolved rotational spectra, and a more detailed study of dimer rovibrational temperature dependence on laser fluence F was performed. Rovibrational temperatures of absorbing molecules depend on laser fluence, as can be seen from Fig. 6. Figures 6(a) and 6(b) show absorption cavity losses for two different values of F in the wavelength range (668–672) nm. The fluence was changed by changing focusing lens position, giving a different spot surface area on the target. Figures 6(c) and 6(d) represent calculated absorption spectra. The following procedure was employed for temperature determination. A direct fit of calculated absorption cross section to the measured values with input parameters $T_{rot,}T_{vib},N,\Delta\nu$, together with a minimization condition for χ^2 was used:

$$\chi^2=\frac{\sum_{i=1}^{n}[\beta_i^{expt}-\beta_i^{calc}]^2}{n(n-1)}.$$

Here n is the number of points for the fitting procedure which is equal to the number of experimental points. Calculated absorptions for minimized χ^2 are shown in the lower part of Fig. 6. For $F=0.65$ J cm^{-2} the best fit is obtained for $T_{rot}=T_{vib}=200$ K and for $F=1.26$ J cm^{-2}, $T_{rot}=T_{vib}=175$ K. Higher fluence (smaller spot size) gives a higher density of dimers and lower rovibrational temperature. For fluences below 0.25 J cm^{-2}, the molecular absorption could not be observed.

Not only do T_{rot}, T_{vib}, and N depend on F, but also the velocity component in the direction normal to the target surface. Figure 7 shows the influence of laser fluence on the arrival times of lithium atoms (upper part) and dimers (lower part). For these measurements the laser spot area on the target surface was constant (1.6×10^{-2} cm^2) and the energy per pulse was changed. The lines on the figure are only to guide the eye. Arrival times of lithium atoms were found to decrease with increasing F. For larger F values, atoms leave the target surface with a larger amount of kinetic energy. For molecules, the relative velocity change is much smaller however, and depends on the rotational quantum number. In the lower part of Fig. 7 arrival times of lithium molecules in two different rovibrational states $v''=4$, $J''=13$ and $J''=18$ of the $X\,^1\Sigma_g^+$ ground state are shown. Lithium molecules with a smaller rotational number J are faster than those with a higher J number. For fluence below 0.25 J cm^{-2}, the molecular absorption could not be observed. If all of the molecules gain the same amount of kinetic energy when they are ejected from the surface, then it is clear that molecules in higher rotational state will need more time to reach the cavity axis. Therefore each time segment probes a particular part of the molecular ensemble. This is why it appears that the assumption of a Boltzmann rovibrational distribution gives reasonable spectral fits. Therefore the rotational and vibrational temperatures determined correspond to particular molecular velocity subgroups.

The influence of background gas on the vaporized molecules was also examined. Figure 8 shows time evolution of

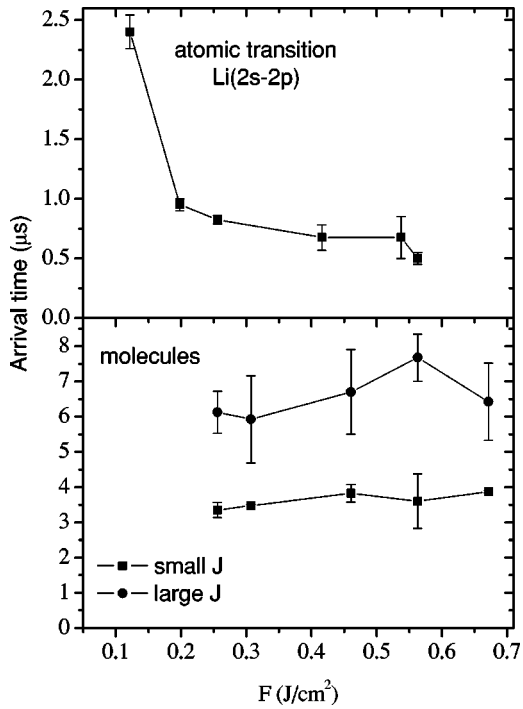

FIG. 7. Observed arrival times of lithium atoms (upper part) and lithium dimers (lower part) vs laser fluence F at $d=1$ cm and angle of incidence equal to 35°. In the lower part of the figure arrival times of lithium molecules in two different rovibrational levels $v''=4$, $J''=13$, and $J''=18$ of the $X\,^1\Sigma_g^+$ ground state are shown.

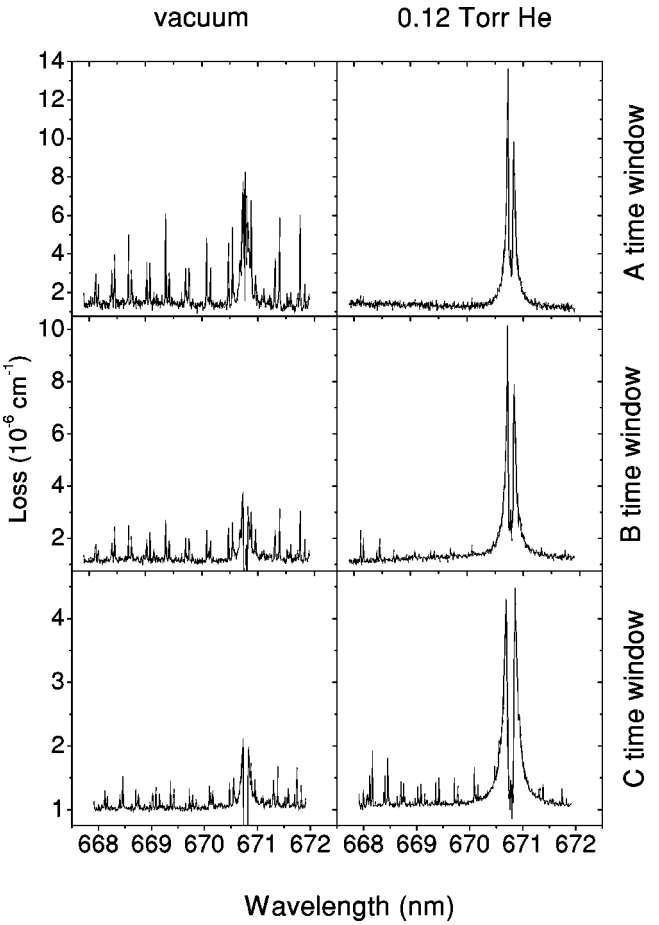

FIG. 8. Time evolution of cavity losses for a pure lithium target in vacuum (left column) and 0.12 Torr of He (right column) at $d=1$ cm and $F=0.8$ J cm^{-2}. Time windows chosen for determination of losses were A(3.75–7.25) μs, first row; B(7.25–13.0) μs, second row; and C(13.0–27.6) μs, third row.

cavity loss measured in the vaporized plume of the lithium target, for vacuum ($<10^{-3}$ Torr) and 0.12-Torr He in the wavelength interval (668–672) nm. Time windows chosen for loss determinations are A (3.75–7.25) μs, B (7.25–13.0) μs and C (13.0–27.6) μs. After the end of the C time window, the slopes of the ring-down curves for off- and on-resonances are equal which means that there are no absorption losses in the cavity. For vacuum, (left column of Fig. 8) the intensity of molecular absorption is highest in time window A and decreases for B and C time windows. On the other hand, for helium background (see the right column of Fig. 8) in time window A molecular absorption is not observed. Dimer appearance is delayed. Weak doublet lines are observed in time window B and the latest time window C contains the largest molecular absorption. Comparison of spectra measured in vacuum and helium leads to the following conclusions: Li_2 dimers are slower in helium than in vacuum, with much smaller intensities of observed molecular absorption. Visual inspection shows that the vaporized plume has a conical shape when it spreads in the vacuum. But, in the case of helium background, the shape changes to spherical and occupies a much smaller volume. Vaporized particles have to push helium atoms away. The temperature in such a spherical plume is increased and under such conditions Li_2 molecules probably dissociate. When the background gas is present, dimers are not observed away from the region of the visible vaporized plume or at a boundary of the visible plume and helium atoms. The atomic line is considerably stronger and line wings are more pronounced due to Stark broadening.

Finally, in Fig. 9 comparison of losses measured in a vaporized plume of (a) pure lithium target, (b) Li/Na alloy, and (c) pure Na target in a wavelength interval (669.9–671.9) nm are shown. This wavelength interval is chosen because it has the smallest overlap between ro-vibrational progressions of the $Li_2(X\,^1\Sigma_g^+\text{-}A\,^1\Sigma_u^+)$ and the $Na_2(X\,^1\Sigma_g^+\text{-}A\,^1\Sigma_u^+)$ electronic transitions with LiNa($X\,^1\Sigma^+$-$A\,^1\Sigma^+$) transition, as evident from the relevant quantum-mechanically calculated absorption cross sections. Clearly, the cavity loss spectra of Li/Na alloy contains lines which are not observed in the loss spectra of pure Li or Na. These lines are therefore assigned to the LiNa($X\,^1\Sigma^+$-$A\,^1\Sigma^+$) electronic transition. In the wavelength interval shown, two rovibrational bands are present, $v''=0\rightarrow v'=4$, 5. The positions of these rovibrational lines are indicated in the upper part of Fig. 9(b). The observed T_{rot} and T_{vib} of LiNa molecules are $\approx$300 K. The densities could not be determined due to the unknown dipole transition moment, but comparison of cavity losses of pure lithium and sodium leads to the conclusion that a similar order of magnitude of LiNa density is observed in the plume.

IV. DISCUSSION

We have observed the Li_2, Na_2, K_2, and LiNa molecules at relatively high densities on the order of 10^{10} cm^{-3}. For

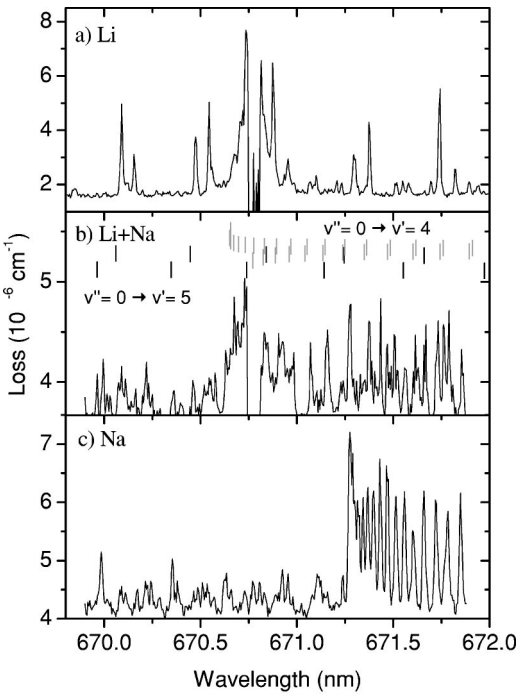

FIG. 9. Cavity absorption losses for normal incidence in vacuum: (a) pure lithium target, $F=0.9\ \mathrm{J\,cm^{-2}}$, $d=2$ cm; (b) Li/Na mixture, $F=0.7\ \mathrm{J\,cm^{-2}}$, $d=1.7$ cm; and (c) pure sodium target, $F=0.7\ \mathrm{J\,cm^{-2}}$, $d=2$ cm. In case (b) calculated positions of rotational-vibrational lines of the LiNa($X\ ^1\Sigma^+ \rightarrow A\ ^1\Sigma^+$) electronic transition are indicated as gray lines for $v''=0\rightarrow v'=4$ and black lines for $v''=0\rightarrow v'=5$.

approximately the same experimental conditions, both atomic and molecular arrival times show square root of mass dependence. This means that different particles gain the same kinetic energy which we could estimate to be about 0.7 eV at a laser fluence of 0.5 J/cm^2. The determined rotational and vibrational temperatures differ slightly from case to case but are lower than room temperature [mainly in (50–200) K interval].

The observed features indicate that molecules are vaporized from the target surface. This is similar to the results of sodium desorption experiments at lower laser fluences by Viereck *et al.* [14]. In the case of molecule formation in the vaporized plume, values of rovibrational temperatures would be higher than observed because of thermalization effects in collisions. For successful molecular formation higher densities are preferred. We observed that if ablation is performed in a helium background, Li_2 molecules are delayed and produced with smaller yield than under vacuum condition. The interpretation is that molecules of background gas confine the ablated species in a smaller volume and the density and temperatures inside the ablation plume increase. If dimers are formed during different collision processes in the gas phase, then the amount of molecules should be larger in the background gas, due to the availability of three-body collisions or relaxation, which is not the case. Furthermore, our observation of LiNa molecules indicates that various dimers could be observed in ablation of properly prepared targets.

Subthermal rovibrational temperatures are the consequence of a jetlike expansion of vaporized molecules. As was already observed, rovibrational temperatures of lithium dimers are different in different time windows across the ring-down curve [15] and depend on F. The fastest dimers appear with the smallest temperatures. When the laser pulse hits the target surface, it creates a small crater through which the ablated atoms and molecules expand into the vacuum. If the spot surface of the laser pulse on the target is larger, observed rovibrational temperatures are higher, because the depth of the crater in the target becomes smaller and the effect of rovibrational cooling decreases. Such relatively large densities of dimers with small rovibrational temperatures could be suitable for loading in different molecular traps. For example, to obtain a lithium molecular number density of $10^{10}\ \mathrm{cm^{-3}}$ by thermal heating sample, temperatures of 700 K are needed.

Using CRDS we succeeded in observing molecules in the ablation plumes which is not possible through emission measurements. This method is very powerful and can be applied across a wide range of densities and in different experiments. Even smaller densities (for example, $10^6\ \mathrm{cm^{-3}}$), could in principle be detected using higher reflectivity mirrors and choosing spectral transitions with larger absorption cross sections. For example, the largest Franck-Condon factors of the Li_2, Na_2, and K_2 transitions are around 665.88 nm ($v''=0\rightarrow v'=4$ progression), 642 nm ($v''=0\rightarrow v'=8$ progression) and 644.32 nm ($v''=0\rightarrow v'=2$ progression). We calculate that R must be 99.9997% (which is accessible for red spectral region) in a given experimental setup. In addition, time resolved CRDS could be used in the detection of condensation processes in the vapor cloud appearing above heated materials [41], starting at much lower temperatures.

V. CONCLUSIONS

By analyzing ring-down curves in properly chosen time windows we observed atoms and dimers in laser ablated plumes of alkali metals. We determined Li_2, Na_2, and K_2 densities in the range from 10^8–$10^{10}\ \mathrm{cm^{-3}}$, with internal temperatures in the range 50–200 K. Here we have demonstrated that pulsed laser ablation of carefully prepared targets together with time-resolved CRDS is a promising method for the formation and characterization of different molecules with subthermal rovibrational temperatures. We believe that use of the CRDS technique as compared to, for example, laser-induced breakdown spectroscopy could bring further advances in the understanding of laser induced plumes.

ACKNOWLEDGMENTS

This work was financially supported by the Ministry of Science and Technology of the Republic of Croatia under Contract No. 0035003. We wish to thank Dr. Goran Pichler, Professor Gerard Meijer, and Dr. Giel Berden for valuable discussions.

[1] A.I. Boldyrev, J. Simons, and P. von R. Schleyer, J. Chem. Phys. **99**, 8793 (1993).
[2] D. Azinović, X. Li, S. Milošević, and G. Pichler, Phys. Rev. A **53**, 1323 (1996).
[3] S. Milošević, in *Spectral Line Shapes*, edited by A.D. May, J. R. Drummond, and E. Oks, AIP Conf. Proc. No. 328 (AIP, New York, 1995), Vol. 8, pp. 391–405.
[4] M.E. Fajardo, J. Chem. Phys. **98**, 110 (1993).
[5] T. Götz, M. Bergt, W. Hoheisel, F. Träger, and M. Stuke, Appl. Surf. Sci. **96-98**, 280 (1996).
[6] K. Vaskonen, J. Eloranta, and H. Kunttu, Chem. Phys. Lett. **310**, 245 (1999).
[7] E. Tognoni, V. Palleschi, M. Corsi, and G. Cristoforetti, Spectrochim. Acta, Part B **57**, 1115 (2002).
[8] P. Bowe, J. Conway, P. Dunne, T. McCormack, and G. O'Sullivan, J. Appl. Phys. **86**, 3002 (1999).
[9] T. McCormack and G. O'Sullivan, Rev. Sci. Instrum. **70**, 2674 (1999).
[10] S. Gogić and S. Milošević, Fiz. A **7**, 37 (1998).
[11] C.W. Huie and E.S. Yeung, Spectrochim. Acta, Part B **40**, 1255 (1985).
[12] T. Götz, M. Bergt, W. Hoheisel, F. Träger, and M. Stuke, Appl. Phys. A: Mater. Sci. Process. **63**, 315 (1996).
[13] J. Viereck, M. Stuke, and F. Träger, Surf. Sci. **377-379**, 687 (1997).
[14] J. Viereck, M. Stuke, and F. Träger, Appl. Phys. A: Mater. Sci. Process. **64**, 149 (1997).
[15] I. Labazan and S. Milošević, Chem. Phys. Lett. **352**, 226 (2002).
[16] A. O'Keefe and D.A.G. Deacon, Rev. Sci. Instrum. **59**, 2544 (1988).
[17] G. Berden, R. Peeters, and G. Meijer, Int. Rev. Phys. Chem. **19**, 565 (2000).
[18] S.S. Brown, A.R. Ravishankara, and H. Stark, J. Phys. Chem. A **104**, 7044 (2000).
[19] A. Czyzewski, K. Ernst, G. Fransse, G. Karasinski, M. Kmieciak, H. Lange, W. Skubiszak, and T. Stacewicz, Chem. Phys. Lett. **357**, 477 (2002).
[20] A.P. Yalin, R.N. Zare, C.O. Laux, and C.H. Kruger, Appl. Phys. Lett. **81**, 1408 (2002).
[21] D. Azinović, I. Labazan, S. Milošević, and G. Pichler, Opt. Commun. **183**, 425 (2000).
[22] L.K. Lam, A. Gallagher, and M.M. Hessel, J. Chem. Phys. **66**, 3550 (1977).
[23] H.-K. Chung, K. Kirby, and J.F. Babb, Phys. Rev. A **60**, 2002 (1999).
[24] B. Barakat, R. Bacis, F.F. Carrot, S. Churassy, P. Crozet, F. Martin, and J. Verges, Chem. Phys. **102**, 215 (1986).
[25] K. Urbanski, S. Antonova, A. Yiannopoulou, A.M. Lyyra, Li Li, and W.C. Stwalley, J. Chem. Phys. **104**, 1 (1996).
[26] I. Schmidt-Mink, W. Müller, and W. Meyer, Chem. Phys. **92**, 263 (1985).
[27] K.K. Verma, M.E. Koch, and W.C. Stwalley, J. Mol. Spectrosc. **87**, 548 (1981).
[28] F.A. van Abeelen and B.J. Verhaar, Phys. Rev. A **59**, 578 (1999).
[29] G. Gerber and R. Möller, Chem. Phys. Lett. **113**, 546 (1985).
[30] W.J. Stevens and M.M. Hessel, J. Chem. Phys. **66**, 1477 (1977).
[31] H.-K. Chung, K. Kirby, and J.F. Babb, Phys. Rev. A **63**, 032516 (2001).
[32] J. Heinze, U. Schühle, F. Engelke, and C.D. Caldwell, J. Chem. Phys. **87**, 45 (1987).
[33] D.D. Konowalow and J.L. Fish (unpublished).
[34] M. Lapp and L.P. Harris, J. Quant. Spectrosc. Radiat. Transf. **6**, 169 (1966).
[35] F. Engelke, G. Ennen, and K.H. Meiwes, Chem. Phys. **66**, 391 (1982).
[36] C.E. Fellows, J. Mol. Spectrosc. **136**, 369 (1989).
[37] M. Harnafi and B. Dubreuil, J. Appl. Phys. **69**, 7565 (1991).
[38] I. Labazan, E. Vrbanek, S. Milošević, and R. Düren (unpublished).
[39] P. Zalicki and R.N. Zare, J. Chem. Phys. **102**, 2708 (1995).
[40] A.P. Yalin and R.N. Zare, Laser Phys. **12**, 1065 (2002).
[41] F.T. Ferguson and J.A. Nuth, III, J. Chem. Phys. **113**, 4093 (2000).